The Thesis committee for Mo Yu

Certifies that this is the approved version of the following thesis:

Tracing the CO "Ice line" in an MRI-active

Protoplanetary Disk With Rare CO Isotopologues

APPROVED BY

SUPERVISING COMMITTEE:

Supervisor: _____

Sarah Dodson-Robinson

_____

Neal J. Evans II

Tracing the CO "Ice line" in an MRI-active Protoplanetary Disk With Rare CO Isotopologues

by

Mo Yu, B.S.

Thesis

Presented to the Faculty of the Graduate School

of The University of Texas at Austin

in Partial Fulfillment

of the Requirements

for the Degree of

Master of Arts

The University of Texas at Austin

August 2013

Acknowledgments

I would like to thank my thesis advisor Sarah Dodson-Robinson for her advising, and the constant support during my entire master study; my collaborator Karen Willacy for providing the chemical network used in this thesis. I want to thank Neal Evans, Anita Cochran, Daniel Jaffe, and John Lacy for being in my research committee, reading research updates and providing inspiring comments throughout this project.

Part of this research was carried out at the Jet Propulsion Laboratory, California Institute of Technology and was sponsored by the National Aeronautics and Space Administration.

Mo Yu

The University of Texas at Austin

August 2013

Tracing the CO "Ice line" in an MRI-active Protoplanetary Disk With Rare CO Isotopologues

by

Mo Yu, M.A.
The University of Texas at Austin, 2013
SUPERVISOR: Sarah Dodson-Robinson

The properties of planet-forming midplanes of protostellar disks remain largely unprobed by observations due to the high optical depth of common molecular lines and continuum. However, rotational emission lines from rare isotopologues may have optical depth near unity in the vertical direction, so that the lines are strong enough to be detected, yet remain transparent enough to trace the disk midplane.

In this thesis, we present a chemical model of an MRI-active protoplanetary disk including different C, O isotopes and detailed photochemical reactions. The CO condensation front is found to be at 1.5 AU on the disk midplane around a solar like star, and its location remains almost unchanged during 3 Myr of evolution. The optical depth of low-order rotational lines of $C^{17}O$ are around unity, which suggests it may be possible to see into the disk midplane using $C^{17}O$. Such ALMA observations would provide estimates of the disk midplane temperature if the CO ice lines were spatially or spectrally resolved. With our computed $C^{17}O/H_2$ abundance ratio, one would also be able to measure the disk masses by measuring the intensity of gas emission.

Contents

Chapter 1

Introduction

The temperature, density and composition of protoplanetary disks determine materials available for planet formation. However fundamental properties of protostellar disks such as midplane temperature, turbulent viscosity, and disk mass are currently poorly constrained by observations. Here we seek a molecule that can be used to probe protostellar disk midplanes. It must be present in the gas phase, even in a cold disk, and be optically thin enough so that the disk is transparent in its rotational line emissions. Finding such a molecule would allow mass estimates in the planet-forming region as well as disk thermometry using the location of the ice line.

Ices formation increases the total solid available for planet formation; the location of ice condensation fronts can also be used as tracers of disk temperatures (Dodson-Robinson et al., 2009). Ice condensation fronts can be identified by the drop of gas emission intensity due to freeze-out in spatially resolved molecular line

maps (Qi et al., 2011), or from the absence of low velocity components in a resolved spectral line. While water, methane, and ammonia ices are more important for planet formation, condensation fronts of more volatile molecules such as CO should be present further out from the central star, therefore potentially resolvable with ALMA for nearby star-forming regions.

Rotational emissions from isotopically common CO molecules are optically thick due to their high abundances and low excitation energies. Isotopically rare molecules may provide optically thin lines due to their low abundances. The energy needed to excite CO molecules before dissociation is slightly different for each isotopologue due to small mass differences. While UV radiation that can dissociate regular CO molecules is sufficiently damped just below the disk surface, rare isotopologues may suffer from more photodissociation because the self-shielding is less efficient. Lyons & Young (2005) have shown that differential photodissociations of CO isotopologues may help to explain the equal fractionation of ^{17}O and ^{18}O in meteorites. We therefore require chemical models of protostellar disks that include photochemistry to ensure that disks contain enough rare isotopologues of CO to be detectable in rotational lines.

In this thesis, we construct chemical evolution models of T-Tauri disks including different C, and O isotopes, with treatments of photochemical reactions. We identify isotopologues of volatile molecules, which are abundant enough to be

observed in the submillimeter, yet whose emission lines still remain optically thin enough to trace disk midplanes.

We build our chemical evolution model upon those of Magnetorotational Instability - active disks (Balbus & Hawley, 1991, here after MRI,) from Landry et al. (2013), which include a viscosity prescription for accretion driven by MRI turbulence, and compare the results in MRI-active disks with a well-adopted model in the literature (D'Alessio et al., 2006). In Chapter 2, we outline the setup and thermal structure of the disk evolution model our chemical model is built upon. We present the isotopic chemical network and the results in Chapter 3 and 4, then evaluate the possibility of using a $C^{17}O$ line to probe ice condensation fronts in the disk midplane in Chapter 5. After we discuss the potential and limits of this study in Chapter 6, we summarize the main results in Chapter 7.

Chapter 2

Disk Thermal Dynamical Models

2.1 $1+1$ D dynamical evolution models driven by the MRI turbulence

Landry et al. (2013) calculated the $1+1$D structure of low mass T-Tauri disks as a function of time under axisymmetric, geometrically-thin disk assumptions. The disks contain $0.03\,M_\odot$ and $0.015\,M_\odot$ within 70 AU of the star at the beginning of the evolution. While the inner edge of the disk is set at 0.5 AU, the outer edge of the disk is allowed to expand as the disk dissipates. The disk model follows the evolution track of a $0.95\,M_\odot$ star (D'Antona & Mazzitelli, 1994) from 0.1 Myr (Dunham & Vorobyov, 2012), roughly the beginning of the T-Tauri phase, to 3 Myr. The input parameters are listed in Table 2.1.

Table 2.1 Basic Parameters of the disk model

	0.1 Myr	3 Myr	α disk [1]
Σ_0 (gcm^{-2}) [2]	2.77×10^3	2.77×10^3	
$M_\star$ ($M_\odot$)	0.95	0.95	0.7
$T_\star$ (K)	4600	4500	4000
$R_\star$ ($R_\odot$)	5.5	1.5	2.5

[1] Parameters used in D'Alessio et al. (2006)
[2] Σ_0 is the surface density at 1 AU. Σ_0 is $2.77 \times 10^3 gcm^{-2}$ in the $0.03\,M_\odot$ disk, and $1.39 \times 10^3 gcm^{-2}$ in the $0.015\,M_\odot$ disk

At each time step, the radial structure is calculated with the diffusion equation:

$$\frac{\partial \Sigma}{\partial t} = \frac{3}{R}\frac{\partial}{\partial R}\left[R^{1/2}\frac{\partial}{\partial R}\left(\Sigma \bar{\nu} R^{1/2}\right)\right], \tag{2.1}$$

with the radial diffusion coefficient $\bar{\nu}$ of:

$$\bar{\nu} = \frac{2}{\Sigma}\int_{z=0}^{z_{surf}} \nu \rho dz. \tag{2.2}$$

The vertical structure is then calculated independently at each radius. We assume the gas and dust are well mixed. The dust has undergone some degree of grain growth, with a grain size of 1μm (Oliveira et al., 2010) and gas to small dust mass ratio of 1000. To preserve the canonical gas to solid ratio of 100, the remaining solids are locked into larger bodies (Dodson-Robinson & Salyk, 2011).

The thermal structure of the disk influences the chemistry at each individual grid cell. The disk is heated by stellar irradiation, background radiation from the

remnant molecular cloud and viscous heating. The degree of viscous heating depends on whether MRI is active in that particular zone. At each grid point, the Ohmic resistivity η_O and ambipolar diffusitivity η_A are determined from a look-up table based on the gas temperature T, density ρ, ionization rate ζ, and plasma β, following Flaig et al. (2012).

If $\eta_A > \eta_O$, ambipolar diffusion dominates. MRI is active when (Bai, 2011):

$$\beta > \beta_{min}, \tag{2.3}$$

where plasma β is the ratio of gas pressure to magnetic pressure:

$$\beta = \frac{8\pi P}{|B|^2}, \tag{2.4}$$

and β_{min} is:

$$\beta_{min}(Am) = \left[\left(\frac{50}{Am^{1.2}}\right)^2 + \left(\frac{8}{Am^{0.3}} + 1\right)^2\right]^{1/2}. \tag{2.5}$$

Am is the ratio of fastest-growing wavelength to the ambipolar diffusive scale length:

$$Am = \frac{v_A^2}{\eta_A \Omega}. \tag{2.6}$$

In Equation 6, v_A is the Alfven velocity, and Ω is the angular velocity of the Keplerian disk.

If $\eta_A < \eta_O$, the Ohmic resistivity dominates. MRI is active when:

$$\Lambda = \frac{v_{AZ}^2}{\eta_O \Omega} \geq 1, \tag{2.7}$$

where v_{AZ} is the Alfven speed in the vertical direction. Physically, the Elsasser number (Λ) is the ratio of the fastest-growing wavelength of perturbation to the diffusion lengthscale. This criteria ensures that the most unstable mode can grow more quickly than charged particles can diffuse across magnetic field lines.

The equilibrium temperature (T_{eq}) at the disk surface contributed by passive heating by the star is evaluated following D'Alessio et al. (2006), and the true temperature T is the flux sum of the accretional temperature T_{acc}, equilibrium temperature (due to passive heating from the central star) T_{eq}, and the ambient temperature T_{amb} contributed by long wavelength heating penetrating into the disk from the environment:

$$T^4 = T_{acc}^4 + T_{eq}^4 + T_{amb}^4. \tag{2.8}$$

2.2 MRI model results

The disk has an MRI active layer on the surface, which provides an accretion rate of $10^{-9}\, M_\odot/yr$ even when a dead zone is present. We see the MRI shut down by Ohmic resitivity on the midplane, forming a deadzone extending from about 2 AU to 16 AU in the $0.015\, M_\odot$ disk, and 3 AU to 21 AU in the $0.03\, M_\odot$ disk. The midplane

temperature reaches $T_{amb} \approx 20K$ as close as about 2 and 3 AU to the star in each disk due to the beginning of deadzone, and rises moderately at the end of dead zone. The temperature decreases smoothly with radius on the disk surface due to the decrease of stellar irradiation, presenting a significant vertical temperature gradient at each radius. The temperature map of the $0.015\,M_{\odot}$ disk at the beginning of the evolution is shown in Figure2.1.

In both cases, the vertical size of both the dead zone and the entire disk shrinks as the disk evolves, but the radial extent of the deadzone remains the same. The temperature on the disk surface decreases due to the star evolving across the Hayashi track, but the temperature on the disk midplane doesn't change much (Landry et al., 2013, see Figure 7). Some part of the deadzone can slightly heat up when matter piles up. In contrast, in a disk with a constant α value, the midplane temperature will first cool off due to the stellar evolution then heat up again when the inner disk becomes optically thin to the stellar irradiation. For the chemical evolution model, the difference between a cooling disk and one that heats in selected zones is important.

2.3 Comparison with an alpha disk model

In order to compare the MRI disk results with predictions from other models, we construct a chemical evolution model upon the disk model from D'Alessio et al.

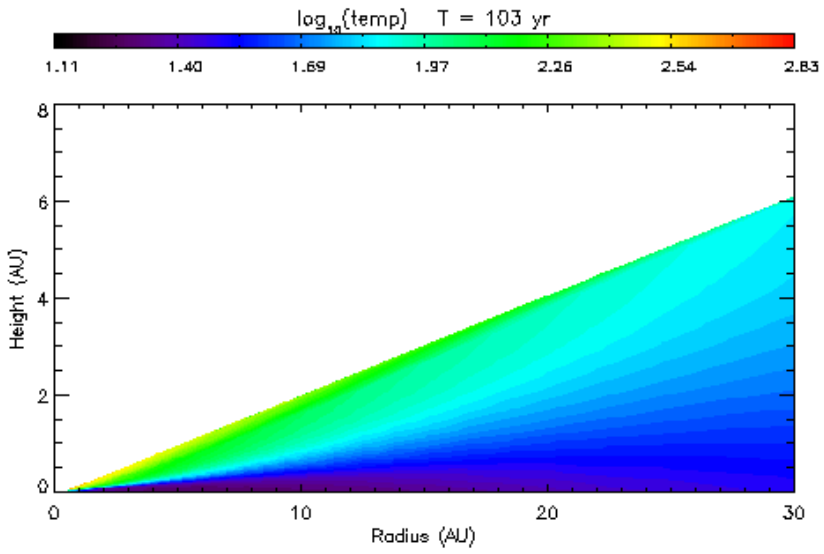

Figure 2.1 Disk temperature map of the MRI disk ($0.015\,M_{\odot}$)

(2006) with a constant α value (Shakura & Sunyaev, 1973) of 0.01 (see Table 2.1 for details).

Temperature structure of the α disk model is shown in Figure2.2. Unlike in the MRI disk models where viscous heating is shut down due to the formation of the dead zone, viscous heating is effective throughout the disk, contributing to a disk midplane significantly hotter than in the MRI disk models. (We are having some problems with the interpolation in the IDL contour routine, and the hot surface is pure artificial).

It is worth noticing that the stellar luminosity at the beginning of our MRI-

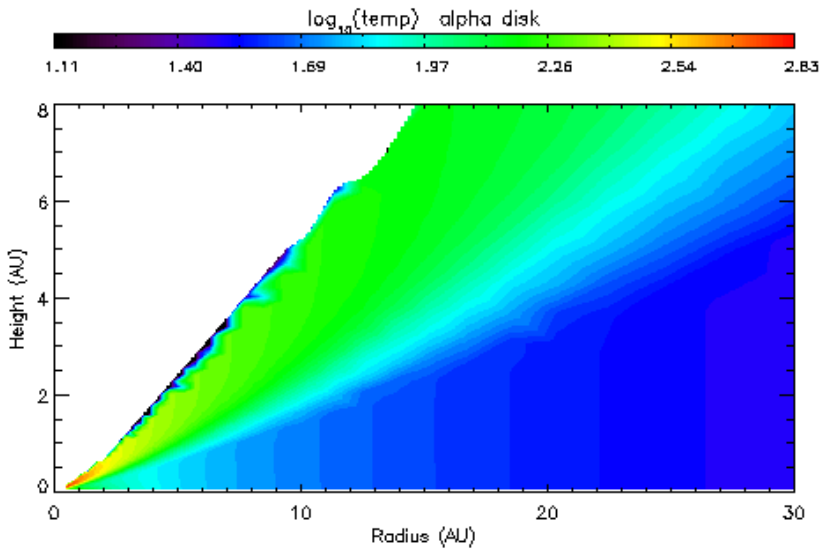

Figure 2.2 Disk temperature map of the alpha disk (We are having some problems with the interpolation in the IDL contour routine, and the hot surface is not real)

active evolution models (0.1 Myr) is 8.4 times the value used in the α disk model. As the star contracts and evolves along the Hayashi track, the luminosity drops to about 0.6 times the α disk value at 3 Myr.

Chapter 3

Chemical model setup

We construct detailed chemical evolution models including different C, and O isotopes based on the UMIST database RATE95 (Millar et al., 1997). The model includes gas phase reactions, grain surface reactions, freeze out, thermal desorptions, and reactions triggered by UV, Xray and cosmic-rays, such as isotope-selective photodissociations.

In order to calculate the chemical evolution over a $3Myr$ lifetime, we use rate equations to calculate reaction rates under the "mean field" approximation (Willacy et al., 2006; Garrod & Herbst, 2006). For gas-grain reactions, where the number of reacting particles per grain is typically less then one and the mean field approximation breaks down, we use modified rate equations to take into account the stochastic effects. Our treatment of grain surface reactions, freeze-out, and thermal desorptions is similar to that of Dodson-Robinson et al. (2009), only with

updated correction factors for the stochastic effects. Therefore we only focus on the treatment of photochemical reactions in this thesis.

We calculate the chemical evolution at each grid point independently. By doing this, we assume the radial and vertical motions of gas and dust are slow compared to chemical reaction timescales, and the mixing is not important in determining the chemistry, an assumption that will be revisited in future work.

3.1 Preprocessing in the molecular cloud

We model the chemical evolution in the molecular cloud stage and use it as the input for the protoplanetary disk models. The molecular cloud model starts from 9 species, with one in the ionic form (C^+), and 8 in the atomic form. The input abundances are listed in Table 3.1. The input C/^{13}C ratio is 77.15; O/^{18}O ratio is 500; and O/^{17}O ratio is 2300. Molecules are formed as we gradually decrease the temperature of the cloud. At the end of the molecular cloud evolution, most of carbon atoms are locked in ices, and most of carbon in gas phase is contained in CO molecules (see Table 3.1). The CO/^{13}CO ratio in gas phase is around 46 at the end of the molecular cloud evolution, , and the CO/^{13}CO ratio in ice is about 63.

Table 3.1 Input abundances of the molecular cloud model

Element	Abundance [1,2]	Element	Abundance
H	1.0 (-2)	He	1.4 (-1)
C^+	7.2 (-5)	$^{13}C^+$	9.3 (-7)
O	1.8 (-4)	^{18}O	3.5 (-7)
^{17}O	7.6 (-8)	N	2.1 (-5)
Si^+	3.0 (-9)		

[1] number density with respect to the total proton number density
[2] A(B) stands for A$\times 10^B$

Table 3.2 Output abundances of the molecular cloud model

Ice	Abundance [1]	Gas	Abundance
CO_2	3.2 (-5)	CO	1.9 (-6)
CH_4	2.2 (-5)	^{13}CO	4.2(-8)
CO	1.3 (-5)	CH_x [2]	1.3 (-7)
^{13}CO	2.9 (-8)	CO_2	6.5(-11)

[1]Notations are the same as in Table 3.1.
[2]Hydrocarbon that contains only one carbon atom.

3.2 UV ionizations, dissociations and desorptions

UV radiations can ionize and dissociate species in the gas phase, and desorb ice from the grain surface.

We consider the stellar UV radiation shining parallel to the disk midplane, which is 500 times the local interstellar value (LISM) at 100 AU, appropriate for a $G0$ star. The radiation flux on the disk surface decreases as r^{-2} from the star. At a distance of r from the central star, and z above the midplane, the radiation field

is (in the unit of local interstellar radiation field):

$$F_{UV}(r,z) = 500 \times \left(\frac{100AU}{r}\right)^2 e^{-\beta A_v}. \tag{3.1}$$

The UV radiation is attenuated exponentially with extinction (A_v) - $e^{-\beta A_v}$ - as it penetrates into the disk (Tielens & Hollenbach, 1985), where β is a scaling factor relating the visual extinction to the extinction at wavelength relevant to each reaction (which is 1.8 for H_2O photodesorptions). The visual extinction (A_v) correlates with the total H_2 column density as:

$$\begin{aligned} A_v &= 5.2 \times 10^{-22} \times N(H_2) \\ &= 5.2 \times 10^{-22} \times \frac{f_H \Sigma_r}{2 m_H}, \end{aligned} \tag{3.2}$$

where $f_H = 0.735$ is the H number fraction out of the total proton number. In order to calculate the attenuation of the stellar irradiation parallel to the disk midplane, we use the horizontal column density integrated from the inner edge (r_{in}) where stellar radiation reaches the disk surface

$$\Sigma_r(r,z) = \int_{r_{in}}^{r} \rho(R,z) dR \tag{3.3}$$

to calculate the extinction.

For photodesorptions, the reaction rate is calculated by (Hollenbach et al.,

2009):

$$k(r,z) = F_{uv}(r,z) \times 10^8 \times (\pi a^2) \times pd_{yield} \tag{3.4}$$

where 10^8 is approximately the local interstellar FUV radiation with photon energy between 6 and 13.6 eV. πa^2 is the cross section of the dust grain where the grain diameter a is taken as 0.258μm.

pd_{yield} is the photodesorption yield (molecule/photon), which is measured in laboratory for H_2O photodesorption by $Ly\alpha$ photons (Westley et al. 1995a, b). The pd_{yield} for H_2O is found to be decreasing with lower grain surface temperature. However because of the lack of measurements for other molecules, we take a constant pd_{yield} value of 10^{-3} for all photodesorptions.

For photoionizations and photodissociations of molecules except CO and H_2, the reaction rate is calculated by:

$$k(r,z) = f F_{UV}(r,z) \tag{3.5}$$

where f is the reaction rate from the LISM field. The radiation is attenuated similarly to that for photodesorption, only with slightly different damping coefficients for different reactions (on the order of unity).

3.3 X - ray photoionization

X-rays can strongly ionize the disk, but only efficiently on the very surface layer due to the rapid attenuation by dust absorptions. By considering both the Compton scattering and photoelectric absorptions, Igea & Glassgold (1999) have shown that at a fixed radius from the source, the X-ray ionization rate is a universal function of the vertical column density, independent of the detailed structure of the disk. We follow the prescription of X-ray ionization of Bai & Goodman (2009):

$$k = L_{X,29}\left(\frac{1AU}{r}\right)^{2.2}\left[\zeta_{abs}\left(e^{-\left(\frac{\Sigma_{up}}{2.5\times10^{-3}}\right)^{0.4}}+e^{-\left(\frac{\Sigma_{dw}}{2.5\times10^{-3}}\right)^{0.4}}\right)\right. \\ \left.+\zeta_{sca}\left(e^{-\left(\frac{\Sigma_{up}}{1.2}\right)^{0.65}}+e^{-\left(\frac{\Sigma_{dw}}{1.2}\right)^{0.65}}\right)\right] \tag{3.6}$$

where $\zeta_{abs} = 6\times10^{-12}s^{-1}$ is the ionization rate for direct absorption, and $\zeta_{sca} = 10^{-15}S^{-1}$ is the ionization rate for scattered photons. The coefficients are for the $3keV$ case in Igea and Glassgold's simulation, and the dependence on photon energy is shown to be weak in the range relevant to disks around solar-like stars. Σ_{up} and Σ_{dw} are the vertical column density from the top and bottom layers of the disk. Since we are only modeling one quarter of the disk, Σ_{dw} is calculated by: $\Sigma_{dw}(r,z) = 2\Sigma_{up}(r,z=0) - \Sigma_{up}(r,z)$. $L_{X,29}$ is the stellar X-ray luminosity in units of $10^{29}ergs^{-1}$. We take $L_{X,29} = 20$ as observed by Chandra observation of solar mass young stars in Orion Nebula (Garmire et al., 2000). However we should bear in

mind that while the X-ray luminosity of solar mass stars is observed to be constant during the first 2 Myr's evolution in the T-Tauri phase, the X-ray luminosity can vary a lot around older stars ($2 - 10$ Myr) (Garmire et al., 2000). The x-ray ionization rate is considered to be the same for all reactions due to the lack of laboratory measurements.

3.4 Cosmic Rays

Cosmic rays can ionize the gas and dissociate molecules by themselves, or with secondary photons.

The intensity of cosmic rays decreases exponentially with the characteristic depth $\Sigma_{cr} = 96 g cm^{-2}$ (Umebayashi & Nakano, 1981) if penetrating perpendicular to the disk. Umebayashi & Nakano (2009) estimated the ionization rate by considering cosmic rays penetrating isotropically from both the top and bottom layers of the disk, and found an ionization rate of:

$$\begin{aligned} k = \frac{k_0}{2}\, e^{-\frac{\Sigma_{up}}{\Sigma_{CR}}} \left[1 + \left(\frac{\Sigma_{up}}{\Sigma_{CR}}\right)^{3/4}\right]^{-4/3} \\ + e^{-\frac{\Sigma_{dw}}{\Sigma_{CR}}} \left[1 + \left(\frac{\Sigma_{dw}}{\Sigma_{CR}}\right)^{3/4}\right]^{-4/3}, \end{aligned} \tag{3.7}$$

where k_0 is the reaction rate under an unattenuated field. As in Eq. 3.6 Σ_{up} and Σ_{dw} are the vertical column density from the top and bottom layers of the disk.

We consider cosmic ray ionizations of 16 species including H_2, He, H, and

the dissociation of H_2 into hydrogen atoms, with unattenuated reaction rates ranging from $3.9 \times 10^{-17} s^{-1}$ to $2.2 \times 10^{-19} s^{-1}$. Cosmic ray ionizations count for most ionizations in the disk midplane and the outer region, where UV and X-ray radiations from the central star are sufficiently attenuated. The ionization of hydrogen molecules contributes the most due to their high abundance,

$$H_2 + CRP \rightarrow H_2^+ + e^-. \tag{3.8}$$

The unattenuated rate for this reaction is $1.2 \times 10^{-17} s^{-1}$ (CRP stard for cosmic ray particles).

The cosmic ray ionization can also generate ionizing photons locally. The cosmic ray induced UV photons can cause ionizations, dissociations and desorptions just as UV photons coming from the central star. Even though the total intensity of cosmic ray induced photons is smaller compared to the stellar radiation, they can still play a role deep into the disk where stellar irradiation is sufficiently damped.

Because the induced photons react locally, we use the same damping factor for cosmic ray induced photons as for cosmic ray particles, only with undamped reaction rates of (Gredel et al., 1989):

$$k_0 = \beta \times \frac{1.3 \times 10^{-17}}{1.0 - \omega}, \tag{3.9}$$

where the albedo ω is 0.5. β is the reaction efficiency with respect to cosmic ray ionizations, which is summed over various electronic states and frequencies, with values ranging from a few tens to a few thousands.

Chapter 4

Chemical model results

4.1 MRI-active disks

The CO condensation front is located at about 1.5 AU on the midplane of the $0.015\,M_\odot$ disk, and at about 2 AU in the $0.03\,M_\odot$ disk. Unlike in the α disk model where ice lines move inward significantly as the disk cools down, the location of the CO ice line on the midplane almost remains unchanged throughout the 3 Myr evolution. The CO abundance is found to be high again at the end of deadzone (15 AU in the $0.015\,M_\odot$ disk, and 20 AU in the $0.03\,M_\odot$ disk), forming an"outer ice line", beyond which CO ice evaporates due to the viscous heating.

At the end of the molecular cloud evolution, roughly 45% of carbon is in CO_2 ice, 30% in methane ice, and 20% in CO ice.

At the end of the 3 Myr disk evolution, CO ice fraction becomes half of its

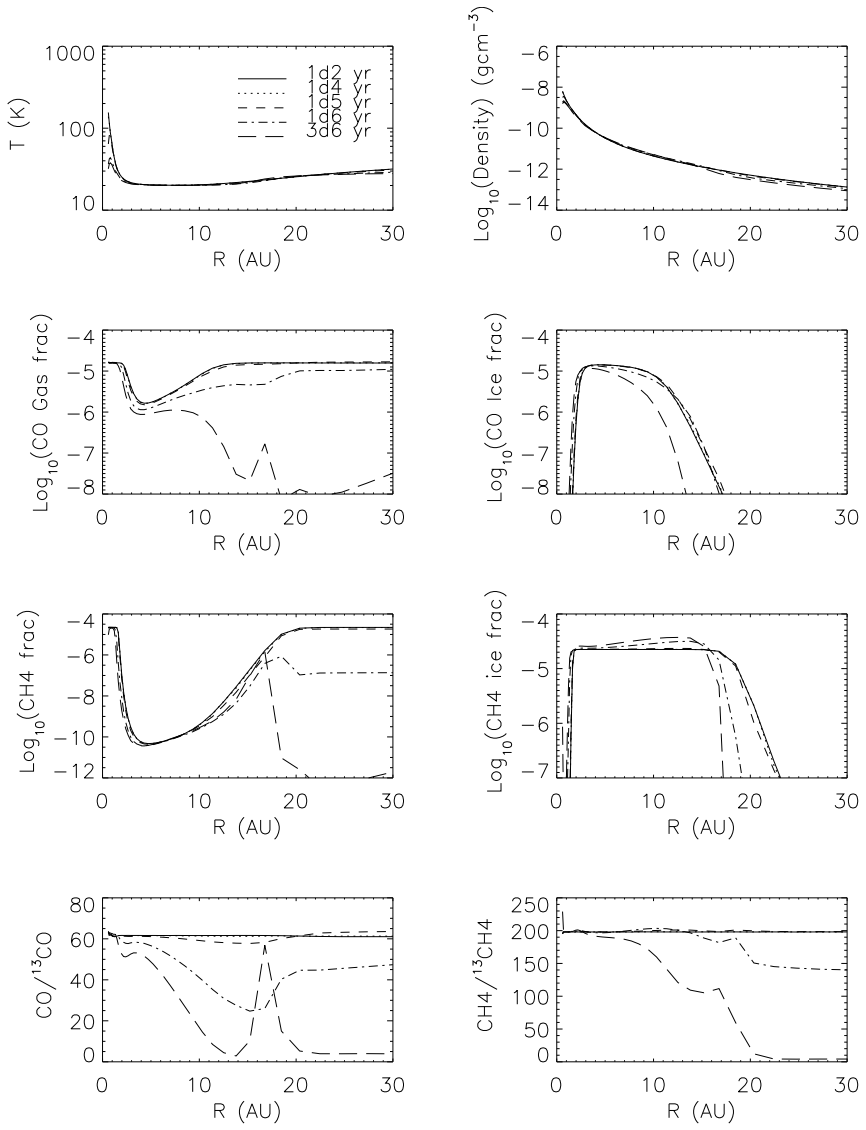

Figure 4.1 Time evolution of the temperature, density, CO, CH4 ice line location and isotopic ratios on the disk midplane

initial value, and the amount of hydrocarbon ice almost doubled. CO gradually changes into hydrocarbon in gas phase then frozen on grains, resulting in a large

decrease in CO abundances. The reaction chain is triggered by Helium ionized by cosmic ray particles (with a small contribution of X-ray).

$$He + CRP \rightarrow He^{+} \tag{4.1}$$

$$He^{+} + CO \rightarrow O + C^{+} + He \tag{4.2}$$

$$C^{+} + H_2 \rightarrow CH_2^{+} + photon \tag{4.3}$$

$$CH_2^{+} + H_2 \rightarrow CH_3^{+} + H \tag{4.4}$$

$$CH_3^{+} + H_2 \rightarrow CH_5^{+} + photon \tag{4.5}$$

$$CH_5^{+} + CO \rightarrow HCO^{+} + CH_4 \tag{4.6}$$

Due to the small reaction rate of cosmic ray ionizations, the hydrogenation hasn't reached an equilibrium until about 1 Myr.

The ion-exchange reaction between C and ^{13}C dominates in determining the

carbon isotopic ratio in CO:

$$^{13}C^{+} + CO \leftrightarrow ^{13}CO + C^{+} + 35K \tag{4.7}$$

Since the forward reaction is energy-favorable, the C^+ to $^{13}C^+$ ratio becomes higher than the cosmic abundance ratio. Reaction 4.7 can be a few hundred times more efficient for C^+ than for $^{13}C^+$, resulting in a low $C/^{13}C$ ratio in CO, and a high $C/^{13}C$ ratio in hydrocarbons.

4.2 Alpha disk

We ran the same chemical network on the alpha disk model, with the UV radiation determined from an Monte Carlo radiative transfer code. Instead of calculating a time evolution model, we ran the chemical network under the same condition for 1 Myr, at which point most reactions have reached equilibrium.

CO doesn't freeze out in our computed region within 32 AU. However C_2Hx ice starts to form at around 8 AU, producing a fake "ice line", mimicking the drop of CO line intensity produced by the CO ice formation.

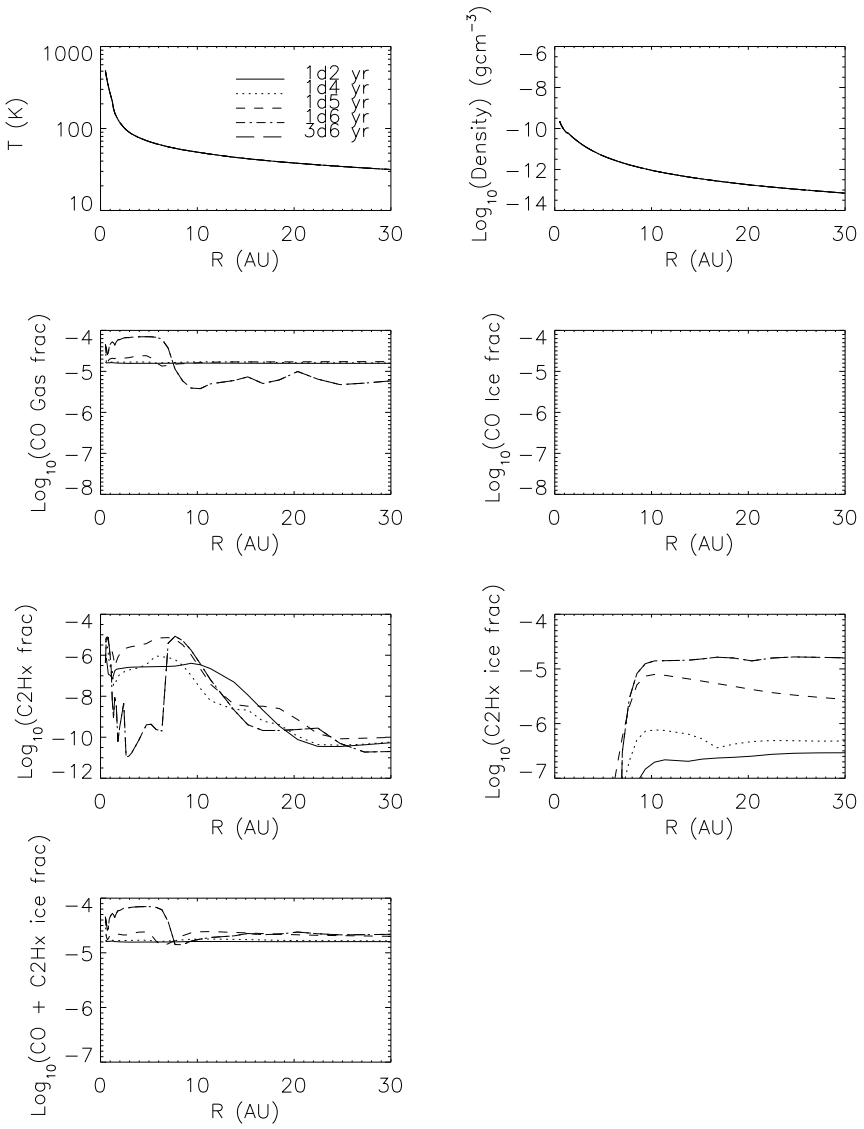

Figure 4.2 Time evolution of the temperature, density, CO, CH4 ice line location and isotopic ratios on the disk midplane in the alpha disk

Chapter 5

$C^{17}O$ as a possible tracer for the disk midplane

5.1 Optical depth estimation

We calculate the optical depth of CO rotational emissions at each radius by integrating the absorption efficiency over the disk height. We first calculate the total absorption efficiency across the line

$$\int k_\nu d\nu = \frac{h\nu_{ij}}{c}\left(n_i B_{ij} - n_j B_{ji}\right), \tag{5.1}$$

in which

$$\begin{aligned} B_{ji} &= \frac{g_i}{g_j} B_{ij}, \\ B_{ij} &= \frac{8\pi^3}{3h^2}|\mu_{ij}|^2, \\ n_i &= f_i n_x. \end{aligned} \tag{5.2}$$

k_ν is the absorption coefficient, n_i, and n_j are the number of molecules in i and j state. f_i, and f_j are the fraction of molecules in i and j state. g_i, and g_j are the degeneracies. ν_{ij} is the frequency of the transition; B_{ij} and B_{ji} are the Einstein coefficients of the transition.

Therefore we have:

$$\int k_\nu d\nu = \frac{h\nu_{ij}}{c} f_i n_x \frac{8\pi^3}{3h^2} |\mu_{ij}|^2 \left[1 - exp\left(\frac{-h\nu_{ij}}{kT}\right)\right], \tag{5.3}$$

where

$$\mathrm{f}_i = \tfrac{1}{Z}\left(2J_i + 1\right) exp\left[\tfrac{-hBJ_i(J_i+1)}{kT}\right], \tag{5.4}$$

and Z is the partition function calculated by

$$Z = \sum_{i=0} \left(2J_i + 1\right) exp\left[\frac{-hBJ_i\left(J_i+1\right)}{kT}\right], \tag{5.5}$$

we truncate the summation at J= 20 because higher levels do not contribute much due to the low temperature.

We divide the total absorption efficiency by the full-width half-maximum (FWHM) of the Doppler broadening profile to estimate the absorption efficiency at the line center

$$\Delta\nu = 2.355 \times \sqrt{\frac{\nu_0^2 kT}{Mc^2}}, \tag{5.6}$$

and integrate the absorption efficiency over the vertical direction

$$\tau = \int_0^{z_{surface}} k_0 dz \tag{5.7}$$

to get the optical depth.

5.2 The optical depth of $C^{17}O$

Optical depths of CO 1-0 lines in the $0.015\,M_\odot$ MRI disk are shown in Figure 5.1. The optical depth decreases as the disk evolves. At 3 Myr the optical depth remains above one until 60 AU for CO, 14 AU for ^{13}CO, and 8 AU for $C^{18}O$. From about 1 Myr, the optical depth of $C^{17}O$ becomes around 1, which means it would be possible to observe the disk mid plane through $C^{17}O$ and constrain the midplane temperature by detecting the CO "snow line".

Optical depths of CO 1-0 lines in the alpha disk model are displayed in Figure 5.2. The optical depth is generally smaller than in the MRI disk model due to smaller disk mass, both $C^{18}O$ and $C^{17}O$ appear to be optically thin at 1 Myr. Although there is no CO ice formations within our modeled region, we still see a drop of line intensity due to the formation of hydrocarbons, which may be misleading if we want to use the drop of the CO gas emission as a tracer for the CO ice formation.

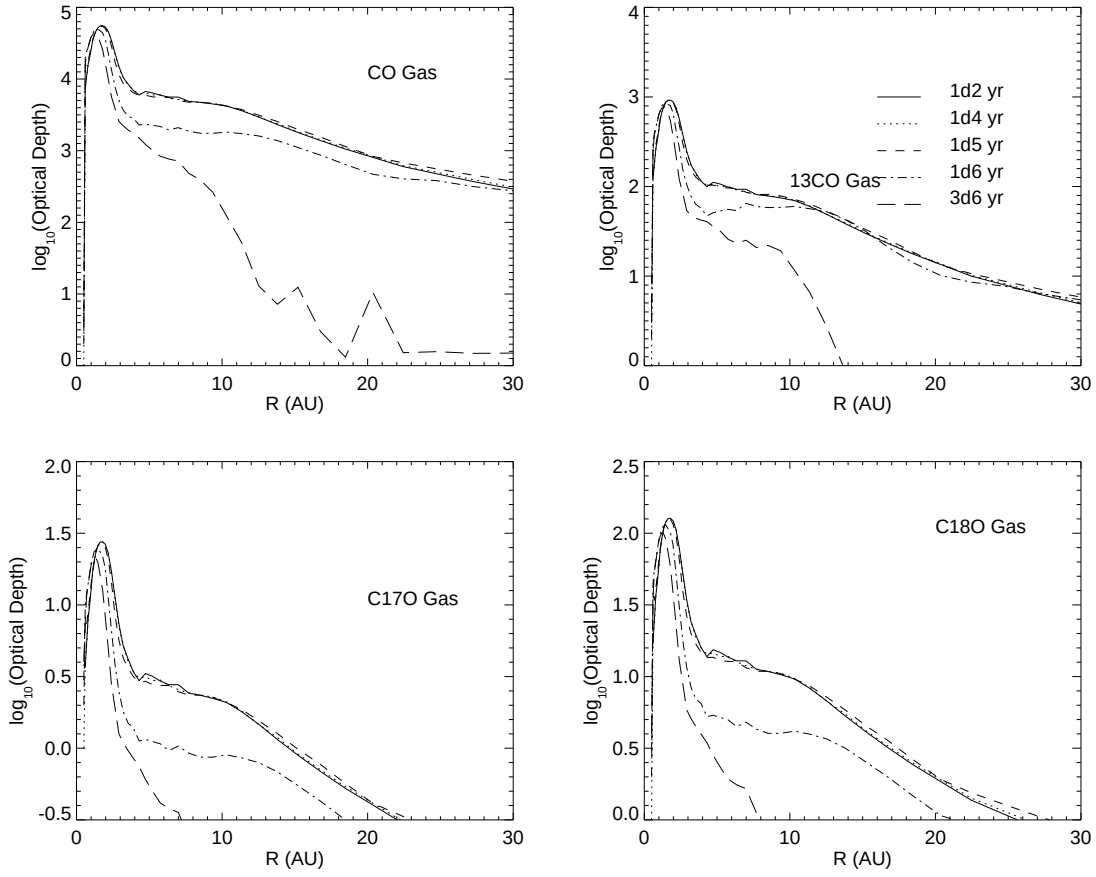

Figure 5.1 Optical depth of CO 1-0 lines (time evolution) in the MRI disk ($0.015\,M_{\odot}$)

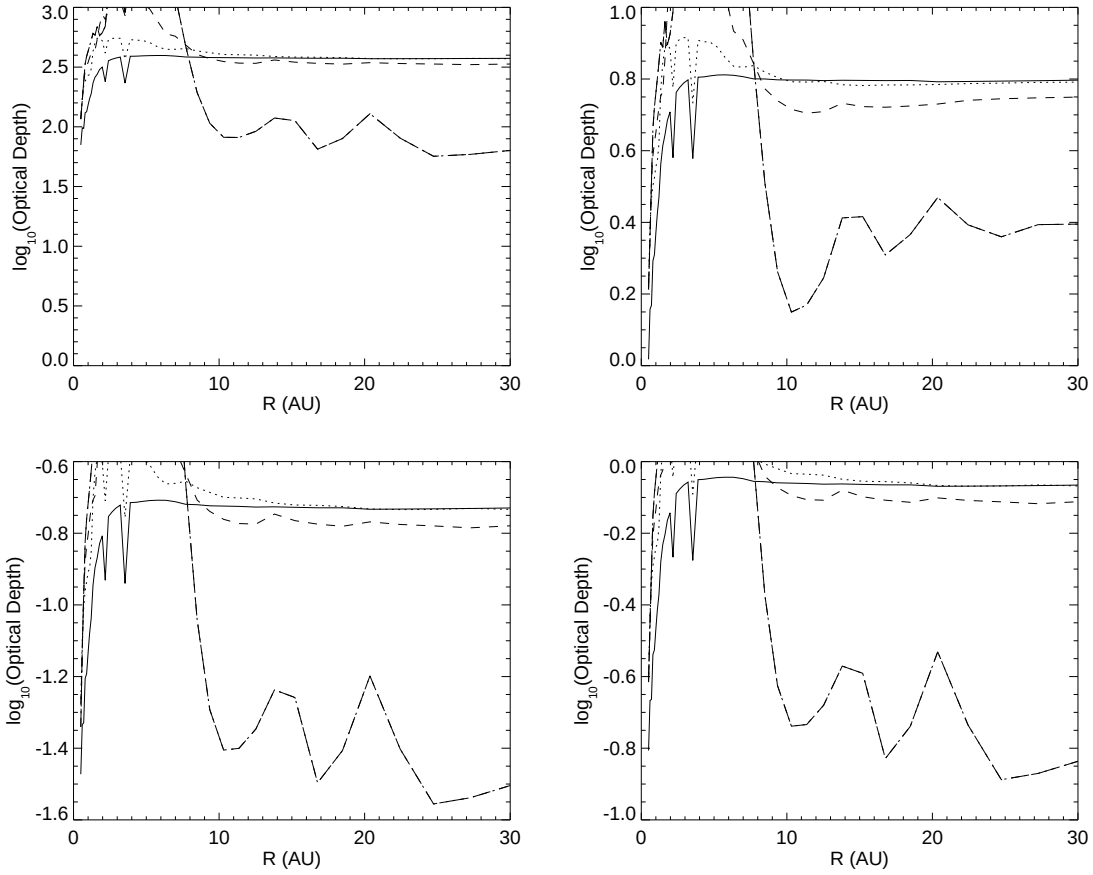

Figure 5.2 Optical depth of CO 1-0 lines (time evolution) in the alpha disk

Chapter 6

Discussion

The optical depth of $C^{17}O$ is found to be around 1 in a low mass protoplanetary disk around a young solar-type star, suggesting it would be possible to use $C^{17}O$ to trace the disk midplane. Ice condensation fronts can be identified by the drop of gas emission intensity due to the freeze-out in spatially resolved molecular line maps, or from the absence of low velocity components in a resolved spectral line. The first method is extremely challenging. For CO 1-0 line at 3 mm, ALMA's resolution in Band 3 is about 80 AU for Taurus (distance 140 pc), which is not enough to spatially zoom into the predicted CO ice line. However, one can learn about the CO ice line location from the emission line shape using the Keplerian rotation. With a larger collecting area of ALMA, one may be able to detect emissions from the inner region of the disk, for example, from 10 AU to the central star with a Keplerian velocity of 9.4 km/s from the line center.

MRI disk models predict very cold midplanes because of the formation of the dead zone, moving the CO ice line to the beginning of the deadzone at about 2 AU from the central star even in a low mass protoplanetary disk. However Qi et al. (2013) found CO freeze-out at 17 K and 30 AU on the disk midplane of TW Hya, using N_2H^+ as a tracer for the CO ice formation. We suspect different dust properties may contribute to this difference. We use a uniform depleted gas to big grain (1μm) mass ratio of 100 in this study; however, further grain growth and settling can increase the degree of heating and ionization, which could potentially produce a hotter midplane by moving the location of the deadzone.

In an alpha disk model, the formation of hydrocarbon can produce a decrease of CO line intensity, mimicking the behavior of the ice formation. Better understanding of the ice content in disks may help to disentangle this problem.

Chapter 7

Summary

In this thesis, we present a chemical model of an MRI-active protoplanetary disk including different C, O isotopes and detailed photochemical reactions. The CO condensation front is found to be at 1.5 AU on the disk midplane around a solar like star, and its location remains almost unchanged during 3 Myr of evolution. In comparison, CO condensation front is found to be at further than 30 AU in a disk with an assumed uniform alpha value of 0.01. However, the formation of hydrocarbon ice can produce a drop in CO emission, mimicking the behavior of the CO ice formation.

The optical depth of low-J rotational lines of $C^{17}O$ are around unity, which suggests it may be possible to see into the disk midplane using $C^{17}O$. Such ALMA observations would provide estimates of the disk midplane temperature if the CO ice lines were spatially or spectrally resolved. With our computed $C^{17}O/H_2$ abundance

ratio, one would also be able to measure the disk masses by measuring the intensity of gas emission.

Bibliography

Bai, X.-N. 2011, ApJ, 739, 50

Bai, X.-N., & Goodman, J. 2009, ApJ, 701, 737

Balbus, S. A., & Hawley, J. F. 1991, ApJ, 376, 214

D'Alessio, P., Calvet, N., Hartmann, L., Franco-Hernández, R., & Servín, H. 2006, ApJ, 638, 314

D'Antona, F., & Mazzitelli, I. 1994, ApJS, 90, 467

Dodson-Robinson, S. E., & Salyk, C. 2011, ApJ, 738, 131

Dodson-Robinson, S. E., Willacy, K., Bodenheimer, P., Turner, N. J., & Beichman, C. A. 2009, , 200, 672

Dunham, M. M., & Vorobyov, E. I. 2012, ApJ, 747, 52

Flaig, M., Ruoff, P., Kley, W., & Kissmann, R. 2012, MNRAS, 420, 2419

Garmire, G., Feigelson, E. D., Broos, P., Hillenbrand, L. A., Pravdo, S. H., Townsley, L., & Tsuboi, Y. 2000, AJ, 120, 1426

Garrod, R. T., & Herbst, E. 2006, A&A, 457, 927

Gredel, R., Lepp, S., Dalgarno, A., & Herbst, E. 1989, ApJ, 347, 289

Hollenbach, D., Kaufman, M. J., Bergin, E. A., & Melnick, G. J. 2009, ApJ, 690, 1497

Igea, J., & Glassgold, A. E. 1999, ApJ, 518, 848

Landry, R., Dodson-Robinson, S. E., Turner, N. J., & Abram, G. 2013, ApJ, 771, 80

Lyons, J. R., & Young, E. D. 2005, Nature, 435, 317

Millar, T. J., Farquhar, P. R. A., & Willacy, K. 1997, A&AS, 121, 139

Oliveira, I., et al. 2010, ApJ, 714, 778

Qi, C., D'Alessio, P., Öberg, K. I., Wilner, D. J., Hughes, A. M., Andrews, S. M., & Ayala, S. 2011, ApJ, 740, 84

Qi, C., et al. 2013, ArXiv e-prints

Shakura, N. I., & Sunyaev, R. A. 1973, A&A, 24, 337

Tielens, A. G. G. M., & Hollenbach, D. 1985, ApJ, 291, 722

Umebayashi, T., & Nakano, T. 1981, PASJ, 33, 617

—. 2009, ApJ, 690, 69

Willacy, K., Langer, W., Allen, M., & Bryden, G. 2006, ApJ, 644, 1202